

Simulation-Based Inference of Ginzburg–Landau Parameters in Type–1.5 Superconductors

Jung-Shen Kao^{1,*}

¹Independent Researcher, Tübingen, Germany

(Dated: December 3, 2025)

Inferring microscopic couplings in multi-component superconductors directly from vortex configurations is a challenging inverse problem. In Type–1.5 systems, time-dependent Ginzburg–Landau (TDGL) dynamics generate complex, glassy vortex patterns with high metastability. We explicitly quantify this intractability by analyzing the Hessian spectrum of the energy landscape, revealing a proliferation of soft modes that hinders traditional sampling. We address this challenge by combining a differentiable TDGL solver with simulation-based inference (SBI). Our approach treats the solver as a stochastic forward model mapping physical parameters $\theta = (\eta, B, \nu)$ to vortex density fields. Using neural ratio estimation (NRE), we train a classifier to approximate the likelihood-to-evidence ratio and perform Bayesian inference for the interband Josephson coupling from vortex density fields. On synthetic data, the proposed method reliably recovers the coupling with calibrated uncertainty intervals. In addition, we analyze the vortex clustering dynamics through the static structure factor $S(k)$, and show that it exhibits a transient suppression of long-wavelength fluctuations in the presence of Andreev–Bashkin drag.

I. INTRODUCTION

Superconductors with multiple intrinsic length scales can exhibit so-called Type–1.5 behaviour [1, 2], where vortex matter shows mixed features of Type–I and Type–II phases. In such systems, intervortex forces can be nonmonotonic and lead to rich clustering patterns, intermediate mixed states, and complex dynamical phenomena. A central theoretical task is to infer the microscopic Ginzburg–Landau (GL) couplings that give rise to these patterns from observable quantities, such as vortex density maps obtained from experiment or numerical simulation.

Time–dependent Ginzburg–Landau (TDGL) equations provide a widely used phenomenological description of the non-equilibrium dynamics of superconducting order parameters. However, the resulting dynamics in multi-component Type–1.5 systems are strongly nonlinear and exhibit glassy dynamics characterized by a rugged energy landscape. In this work, we go beyond qualitative descriptions of metastability by explicitly computing the Hessian eigenvalue spectrum of the vortex configurations. The abundance of near-zero eigenvalues confirms the flatness of the energy landscape. This spectral property has profound implications for inference: it reveals that the likelihood $p(x|\theta)$ is not only analytically intractable but also creates a “flat” optimization surface where local gradients vanish and Markov Chain Monte Carlo (MCMC) walkers become trapped in local basins. Consequently, even with a fully differentiable solver, direct gradient-based inversion remains ill-posed, necessitating a likelihood-free approach.

To overcome these limitations, we adopt the perspective of simulation-based inference (SBI) [3], leveraging

the TDGL solver purely as a stochastic simulator and replacing explicit likelihood evaluations by a learned surrogate. Concretely, we employ neural ratio estimation (NRE) to approximate the likelihood-to-evidence ratio associated with TDGL simulations. The key idea is to train a neural classifier to distinguish samples drawn from the joint distribution $p(\theta, x)$ versus samples from the product of marginals $p(\theta)p(x)$, and to use the classifier output as an estimator for the ratio. We instantiate this idea in a computational framework that couples a JAX-based TDGL solver to a two-branch neural architecture. One branch encodes vortex density fields using a convolutional neural network with global average pooling, naturally enforcing translational invariance. Such architectures act as learnable summary statistics [4], extracting sufficient information from raw physical fields without relying on hand-crafted features.

Importantly, our aim is to bridge the gap between black-box parameter estimation and physical mechanism discovery. In this work we focus quantitatively on recovering a scalar coupling, namely the interband Josephson term, from vortex configurations using NRE. To investigate how more subtle mechanisms such as the Andreev–Bashkin drag effect manifest structurally, we perform an independent analysis of the static structure factor $S(k)$ for simulations with and without drag. This structure-factor analysis reveals that drag induces a transient suppression of large-scale density fluctuations that is invisible to simple static observables, suggesting a dynamical fingerprint that future SBI models could exploit to jointly infer both couplings and drag.

The remainder of the paper is organized as follows. In Sect. II we summarize the GL model and TDGL dynamics underlying our simulations. Section III describes the implementation of the TDGL solver. In Sect. IV we introduce the NRE-based inference scheme and the

* jungshenkao@gmail.com

neural architecture used in our framework. Numerical experiments on parameter recovery for the Josephson coupling, together with a structure-factor-based analysis of the dynamical signature of the drag effect, are presented in Sec. V. We discuss limitations and potential extensions in Sect. VI and conclude in Sect. VII.

II. GINZBURG–LANDAU MODEL AND TIME-DEPENDENT DYNAMICS

The system under study belongs to the class of short-range entangled phases [5, 6] characterized by spontaneous symmetry breaking. Unlike systems with intrinsic topological order, the topological protection here arises from the non-trivial first homotopy group $\pi_1(M) \cong \mathbb{Z} \times \mathbb{Z}$ of the order parameter manifold [7]. The TDGL dynamics thus capture the relaxation of these stable topological defects (vortices) and their interaction-driven clustering.

We consider a two-band superconductor in two spatial dimensions, characterized by complex order parameters $\psi_i(\mathbf{r}, t)$ ($i = 1, 2$) and a magnetic vector potential $\mathbf{A}(\mathbf{r})$. In dimensionless units, the free-energy functional takes the two-component Ginzburg–Landau form:

$$\begin{aligned} \mathcal{F}[\psi_1, \psi_2, \mathbf{A}] = \int d^2r \Bigg\{ & \sum_{i=1}^2 \left[\frac{1}{2} |(\nabla + i\mathbf{A})\psi_i|^2 \right. \\ & + \alpha_i |\psi_i|^2 + \frac{\beta_i}{2} |\psi_i|^4 \Big] \\ & \left. - \eta(\psi_1^* \psi_2 + \psi_1 \psi_2^*) + \frac{1}{2} |\nabla \times \mathbf{A}|^2 \right\}, \end{aligned} \quad (1)$$

where α_i and $\beta_i > 0$ are phenomenological parameters. The term η denotes the interband Josephson coupling, which effectively captures tunneling or impurity scattering derived from microscopic BCS theory [8]. For suitable parameter ranges, this model exhibits a Type-1.5 regime with three fundamental length scales. Microscopically, this leads to a competition between short-range repulsion and long-range attraction, resulting in an effective intervortex potential $V(r)$ resembling a Lennard–Jones potential with a distinct attractive well [1].

We focus on the overdamped time-dependent Ginzburg–Landau (TDGL) dynamics. Importantly, to study the full range of interband interactions, we generalize the standard dynamics to explicitly include the non-dissipative Andreev–Bashkin drag effect, parameterized by the coefficient ν :

$$\begin{aligned} \partial_t \psi_i = D_i (\nabla + i\mathbf{A})^2 \psi_i + \nu (\nabla + i\mathbf{A})^2 \psi_j \\ - \alpha_i \psi_i - \beta_i |\psi_i|^2 \psi_i + \eta \psi_j, \quad i \neq j, \end{aligned} \quad (2)$$

where D_i are diffusion coefficients that control the relaxation time scales. The drag term $\nu (\nabla + i\mathbf{A})^2 \psi_j$ introduces a kinetic coupling between the condensates, representing the entrainment of one superfluid component by the superflow of the other. In this formulation, explicit

thermal noise terms are omitted in the update rule; instead, stochasticity is incorporated via the random initial conditions, representing a rapid quench from the high-temperature normal phase. The terms in Eq. (2) thus describe kinetic energy and drag, magnetic screening, local condensation energy, and the Josephson coupling.

For the simulations reported below, we choose parameters such that band 1 is effectively Type-I-like while band 2 is Type-II-like, leading to a Type-1.5 mixed regime in which vortices tend to form clusters at intermediate fields. Concretely, we work with $\alpha_1 = \alpha_2 = -1$, $\beta_1 = \beta_2 = 1$, and distinct diffusion coefficients $D_1 > D_2$. We treat the Josephson coupling η and the drag coefficient ν as the primary parameters to be inferred from vortex observables, with $\nu = 0$ serving as the baseline for standard interaction models. The external magnetic field strength B (flux per plaquette in the discretized model) is taken as a secondary control parameter.

III. NUMERICAL SIMULATION

To study the non-equilibrium dynamics described by Eq. (2), we employ a finite-difference discretization scheme on a square lattice of size $N \times N$ with physical extent $L \times L$ and grid spacing $dx = L/N$. Numerical stability and gauge invariance are ensured using the link-variable formalism. In the Landau gauge $\mathbf{A} = (0, Bx, 0)$, the vector potential is incorporated via Peierls substitution, where vertical links acquire complex phase factors $U_y(j) = \exp(-iB dx^2 j)$ dependent on the x -coordinate index j , while horizontal links remain real-valued. This construction ensures that the discrete Laplacian converges to the correct gauge-covariant continuum limit as $dx \rightarrow 0$ [9].

The system is evolved in time using an explicit Euler integration scheme. While semi-implicit methods [10] offer superior stability for stiff GL equations, an explicit scheme is chosen here to facilitate seamless integration with automatic differentiation frameworks. Numerical stability is maintained by strictly limiting the time step dt to satisfy the Courant–Friedrichs–Lowy (CFL) condition dictated by the diffusion coefficients D_i . The update rule for a single time step, explicitly including the Andreev–Bashkin drag term, is given by:

$$\begin{aligned} \psi_i^{(n+1)} = \psi_i^{(n)} + dt \Bigg[& D_i \Delta_A \psi_i^{(n)} \\ & + \nu \Delta_A \psi_j^{(n)} - \frac{\delta \mathcal{F}_{\text{loc}}}{\delta \psi_i^*} \Bigg], \quad (j \neq i) \end{aligned} \quad (3)$$

where Δ_A denotes the discrete gauge-covariant Laplacian, ν is the interband drag coefficient parameterizing the non-dissipative kinetic coupling, and \mathcal{F}_{loc} denotes the local free energy density containing the potential and Josephson coupling terms..

Initial conditions are generated by sampling independent uniform noise for the real and imaginary parts of ψ_i at each lattice site, representing a rapid thermal quench

from the disordered normal phase into the superconducting phase. This process dynamically generates a diverse ensemble of metastable vortex configurations driven by the competition between domain formation and topological constraints. To extract physical observables, we compute the gauge-invariant supercurrent density \mathbf{J} and its discrete curl $(\nabla \times \mathbf{J})_z$, which serves as a proxy for the local magnetic field and allows for precise vortex localization.

IV. SIMULATION-BASED INFERENCE WITH NEURAL RATIO ESTIMATION

The TDGL dynamics described above define an implicit stochastic forward model that maps physical parameters $\boldsymbol{\theta} = (\eta, B, \nu)$ to observables x , which we take to be vortex-related fields derived from the long-time TDGL evolution. For a fixed choice of prior $p(\boldsymbol{\theta})$ over the parameters, this induces a joint distribution $p(\boldsymbol{\theta}, x) = p(x | \boldsymbol{\theta})p(\boldsymbol{\theta})$. Since the likelihood $p(x | \boldsymbol{\theta})$ is analytically intractable and expensive to approximate by brute force, we adopt a simulation-based inference (SBI) strategy based on neural ratio estimation (NRE).

The overall workflow, from physics simulation to contrastive training and posterior estimation, is illustrated schematically in Fig. 1.

A. NRE Methodology

The central object in NRE is the likelihood-to-evidence ratio

$$r(\boldsymbol{\theta}, x) = \frac{p(x | \boldsymbol{\theta})}{p(x)} = \frac{p(\boldsymbol{\theta}, x)}{p(\boldsymbol{\theta})p(x)}, \quad (4)$$

which fully characterizes the posterior via

$$p(\boldsymbol{\theta} | x) \propto r(\boldsymbol{\theta}, x)p(\boldsymbol{\theta}). \quad (5)$$

Rather than attempting to model the intractable likelihood directly, we train a neural classifier to distinguish samples from the joint distribution $p(\boldsymbol{\theta}, x)$ from samples drawn from the product of marginals $p(\boldsymbol{\theta})p(x)$. Given a dataset of parameter–observable pairs $\{(\boldsymbol{\theta}_n, x_n)\}_{n=1}^N$ generated by the TDGL solver with parameters sampled from the prior, we construct a contrastive dataset as follows:

- *Positive samples* $(\boldsymbol{\theta}_n, x_n)$ are labeled as $y = 1$ and correspond to draws from $p(\boldsymbol{\theta}, x)$.
- *Negative samples* $(\boldsymbol{\theta}_{\pi(n)}, x_n)$ are created by randomly permuting parameters within each minibatch, labeled as $y = 0$, and approximate draws from $p(\boldsymbol{\theta})p(x)$.

We then train a binary classifier $d_\phi(\boldsymbol{\theta}, x)$ with parameters ϕ to predict y from $(\boldsymbol{\theta}, x)$ using the standard binary cross-entropy loss. In the infinite-capacity limit, the optimal

classifier satisfies

$$d_\phi^*(\boldsymbol{\theta}, x) = \frac{p(\boldsymbol{\theta}, x)}{p(\boldsymbol{\theta}, x) + p(\boldsymbol{\theta})p(x)}, \quad (6)$$

which implies that the learned logit $s_\phi = \text{logit } d_\phi$ approximates the log likelihood-to-evidence ratio up to an additive constant,

$$s_\phi(\boldsymbol{\theta}, x) \approx \log r(\boldsymbol{\theta}, x) + \text{const.} \quad (7)$$

For any given observation x^{obs} we can thus construct an amortized posterior estimator by evaluating s_ϕ over a grid or proposal distribution in parameter space and combining it with the prior.

We choose NRE over other SBI strategies (such as Neural Posterior Estimation via Normalizing Flows) for its robustness in high-dimensional settings. By reformulating density estimation as a binary classification task, NRE leverages the stability of discriminative networks (e.g., CNNs) to handle complex vortex image data, avoiding the training instabilities often associated with flow-based generative models in high-dimensional spaces.

B. Neural Architecture

The neural ratio estimator follows a two-branch architecture tailored to the structure of the data. The observable x is constructed as a **three-channel** field. In addition to the band-resolved densities, we explicitly include the local magnetic field distribution derived from the supercurrent curl, providing the network with direct physical information regarding the magnetic flux topology. The input tensor at each lattice site \mathbf{r} is given by:

$$x(\mathbf{r}) = \left(|\psi_1(\mathbf{r})|^2, |\psi_2(\mathbf{r})|^2, [\nabla \times \mathbf{J}(\mathbf{r})]_z \right). \quad (8)$$

This physics-informed feature engineering ensures that the network has direct access to both the order parameter amplitude (sensitive to η) and the vortex core vorticity (sensitive to B).

This field is processed by a convolutional encoder with several convolution–nonlinearity–pooling blocks. To capture both global texture features (sensitive to η) and sparse vortex core signals (sensitive to B), we employ a dual pooling strategy consisting of Global Average Pooling (GAP) and Global Max Pooling (GMP) in parallel. Crucially, these pooling operations decouple the resulting feature vector size from the spatial dimensions of the input lattice. This design naturally enforces physical translational invariance and ensures resolution independence. Consequently, an encoder trained on a standard discretization grid (e.g., $N = 64$) can directly perform inference on higher-resolution experimental images (e.g., $N = 128$ or higher) without architectural modifications or retraining. This flexibility, not offered by standard flattening-based MLPs, is essential for bridging the gap

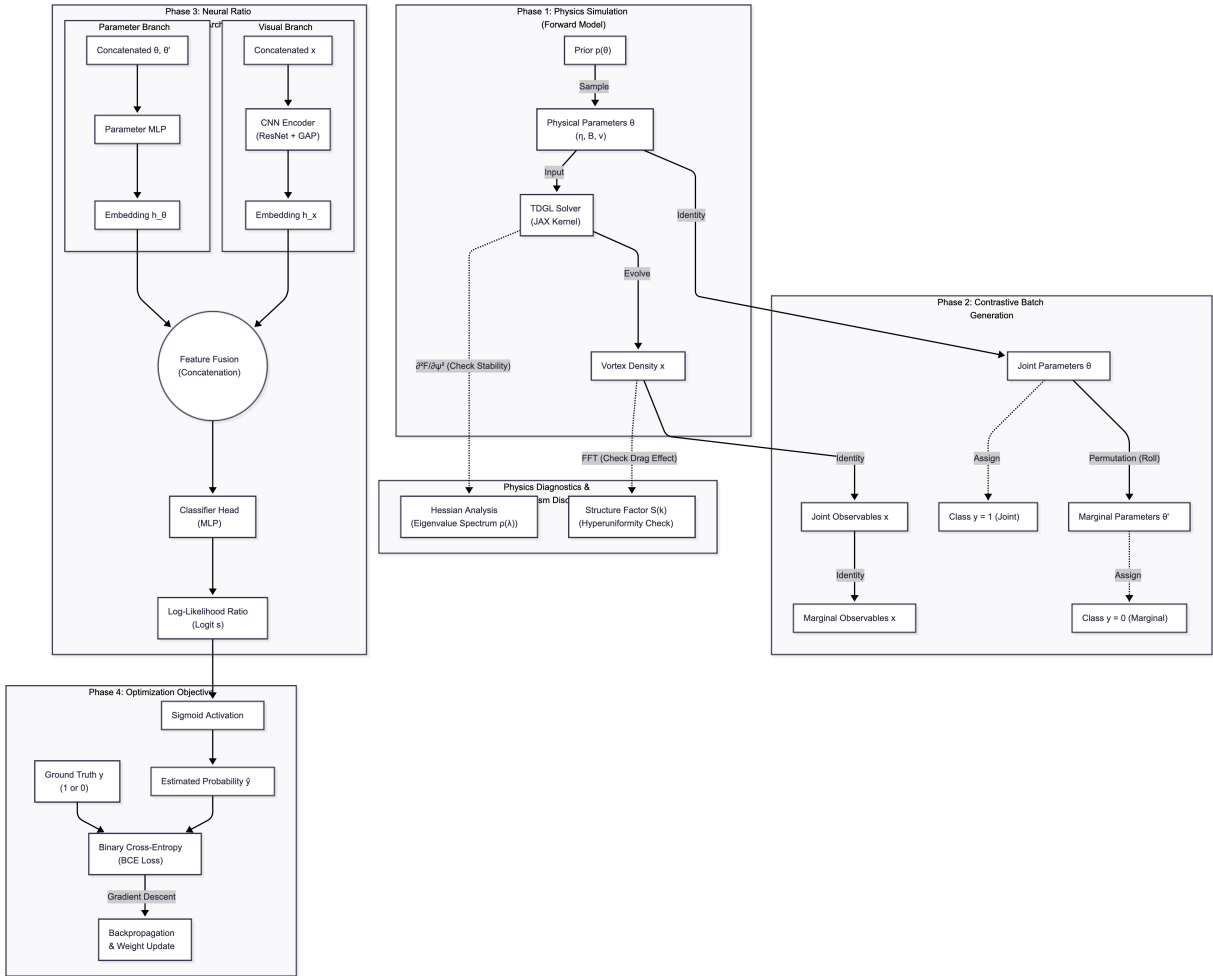


FIG. 1. Overview of the Framework. The pipeline integrates differentiable physics simulation with neural ratio estimation. (Phase 1) A TDGL solver generates vortex configurations from parameters $\theta = (\eta, B, \nu)$. The forward model is augmented with two physical diagnostic loops (dashed lines): Hessian spectral analysis to quantify the ruggedness of the energy landscape (see Sec. A), and structure-factor $S(k)$ analysis to reveal the micro-structural fingerprint of the drag mechanism (see Sec. V C). (Phase 2) A contrastive dataset is constructed on-the-fly by pairing consistent (θ, x) samples (joint) against permuted samples (marginal). (Phase 3 & 4) A two-tower neural architecture fuses visual vortex features with parameter embeddings to approximate the likelihood-to-evidence ratio, trained via binary cross-entropy maximization.

between discrete simulations and high-fidelity experimental data. The final output of this branch is a compact feature vector h_x .

The physical parameters $\theta = (\eta, B, \nu)$ are embedded by a separate multilayer perceptron (MLP) that maps the input parameters to a feature vector h_θ . The two embeddings are then concatenated and passed through a final MLP “head” that outputs a single scalar logit $s_\phi(\theta, x)$. The entire model is implemented in FLAX and trained with the Adam optimizer using a learning rate of 10^{-3} .

V. EXPERIMENTS

We now assess the ability of our approach to recover the Josephson coupling η from synthetic vortex configurations generated by the TDGL solver. In all experiments we fix the GL parameters and diffusion coefficients to the values specified in Sec. II, and treat η as the primary parameter of interest. Unless stated otherwise the external magnetic field is kept at $B = 0.01$ and the lattice size is $N = 64$.

A. Training Setup

For training the neural ratio estimator we draw η from a simple uniform prior over a bounded interval $\eta \sim \mathcal{U}([0, \eta_{\max}])$ and keep B fixed. For each sampled

parameter, we generate an initial condition and evolve the TDGL equations. The resulting dataset of parameter-observable pairs can be streamed online. To ensure scalability to massive ensembles, our framework employs a decoupled offline training strategy where high-resolution simulations are precomputed and stored as compressed datasets. This approach allows the training loop to fully saturate hardware throughput by removing the simulation bottleneck.

B. Posterior Recovery and Quantitative Evaluation

To systematically assess the reliability of our inference framework, we evaluate the trained classifier on a grid of ground-truth coupling values $\eta^* \in [0.2, 1.4]$, covering the transition from weak coupling to the strong single-band limit. The quantitative results are summarized in Table I. We observe a distinct U-shaped trend in the inference error (Fig. 5, left panel), which correlates with the physical identifiability of the vortex patterns.

- **Optimal Regime:** In the intermediate region ($\eta \approx 0.8$), the Mean Absolute Error (MAE) reaches a minimum of 0.011. This corresponds to the regime where Type-1.5 clustering features are most structurally distinct.
- **Boundary Effects:** At the weak ($\eta = 0.2$) and strong ($\eta = 1.4$) coupling limits, the MAE increases to ≈ 0.2 . However, the 95% credible intervals (CI) maintain 100% coverage of the ground truth values.

TABLE I. Quantitative Performance Metrics for Parameter Recovery

True η	Post. Mean	Post. Std	MAE	68% CI Width	95% CI Width
0.20	0.393	0.165	0.191	0.222	1.258
0.50	0.575	0.117	0.075	0.237	1.212
0.80	0.811	0.089	0.011	0.254	1.185
1.10	1.021	0.091	0.079	0.272	1.409
1.40	1.194	0.141	0.206	0.237	1.498

Aggregate Statistics:

Mean Absolute Error (MAE): 0.113 ± 0.076

Coverage (95% CI): 100.0%

For each test case, we compute the posterior score $s_\phi(\eta, x^{\text{obs}})$ and normalize it to obtain the marginal posterior density. Figure 2 displays the resulting distributions. While the above analysis focuses on the marginal posterior of η , the NRE framework naturally captures the full joint posterior $p(\eta, B|x)$, allowing us to examine parameter correlations. As shown in Fig. 3 for the benchmark case of $\eta^* = 0.8$, the inference is highly confident in η , indicated by the narrow width along the horizontal axis. However, it exhibits higher uncertainty in B (vertical elongation). This anisotropy is consistent with the physics of glassy

quench dynamics, where the topological defect density (which proxies for B) is often “frozen in” by the cooling rate rather than perfectly relaxing to the equilibrium flux density. Despite this, the model correctly identifies the parameter region containing the ground truth, demonstrating robustness against non-equilibrium topological variance.

C. Drag Diagnostics from $S(k)$

Beyond scalar parameter estimation, it is important to understand how microscopic mechanisms leave identifiable signatures in mesoscopic observables. Here we focus on the Andreev-Bashkin drag term as a case study and analyze how it modifies the structural correlations of vortex matter. To this end, we compute the radially averaged static structure factor $S(k)$ for ensembles generated with and without the drag term. While both interactions lead to vortex clustering, the drag effect is theoretically predicted to induce a non-dissipative “locking” of the condensates.

We compute the radially averaged static structure factor, $S(k) = \langle |\delta\rho(\mathbf{k})|^2 \rangle$, for ensembles generated with and without the drag term. As shown in Fig. 4, we track the evolution of $S(k \approx 1)$ throughout the quench. Significantly, the inclusion of the Andreev-Bashkin interaction leads to a distinctive suppression of fluctuations in the early relaxation regime ($t < 2.0$), indicating a transient tendency towards hyperuniformity driven by kinetic locking. However, this signature fades as the system approaches the metastable plateau ($t > 3.0$).

This dynamical analysis serves as the physical justification for our choice of inference time $t = 2.0$ in the training phase. By targeting the non-equilibrium window where the kinetic constraint is most active, we obtain observations that are, in principle, informative about drag. In the present work, however, we use $S(k)$ purely as a diagnostic tool and restrict quantitative SBI to the Josephson coupling; extending the NRE to directly infer the drag coefficient is left for future work.

VI. DISCUSSION AND OUTLOOK

A. Physical Interpretation: The Microscopic Meaning of Soft Modes

The proliferation of soft modes (Fig. 6) admits a profound physical interpretation. These modes correspond to **collective vortex rearrangements** where clusters can slide, rotate, or deform with minimal energy cost [11]. Crucially, these are distinct from the standard Goldstone modes arising from continuous symmetries or Anderson-Higgs modes. Instead, they are characteristic **geometrical soft modes** of the Type-1.5 non-monotonic interaction.

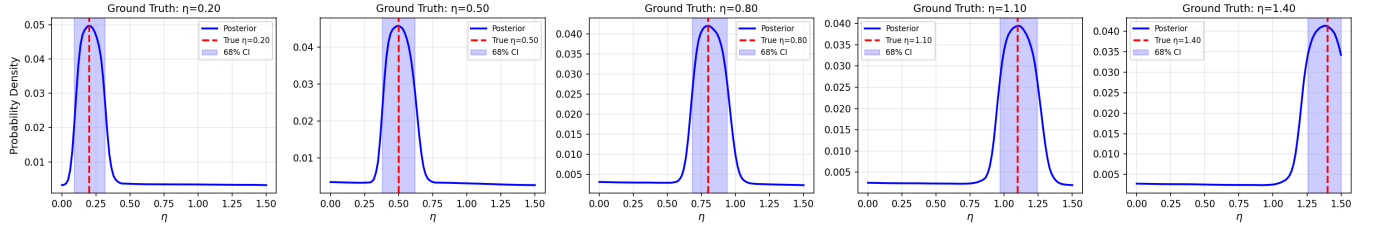


FIG. 2. **Posterior Recovery across Coupling Strengths.** The predicted posterior distributions for five distinct ground-truth values of η . The model accurately localizes the true parameter (red dashed line) within the high-probability region. Note the widening of the posterior at $\eta = 1.4$, correctly reflecting the increased physical ambiguity in the strong-coupling limit.

TABLE II. Mapping between simulation observables and experimental measurements

Experiment	Measured Quantity	Connection to Model
STM	Local density of states (LDOS) at bias voltage V	$\text{LDOS}(E = 0) \propto \psi_1 ^2 + \psi_2 ^2$ (at zero bias, approximately)
Lorentz TEM	Integrated magnetic flux through sample thickness	$\int \mathbf{B} \cdot d\mathbf{A} \propto [\nabla \times \mathbf{J}]_z$ (projection through film)
Neutron scattering	Structure factor $S(k)$ from vortex lattice	Directly comparable to Fig. 5 (coarse-grain to match resolution)
ARPES	Spectral function $A(k, \omega)$ (momentum-energy map)	Requires extension to frequency domain via analytic continuation

It has been theoretically predicted [1] that Type-1.5 systems should exhibit Lennard-Jones-like intervortex potentials $V(r)$ with a characteristic attractive well. Our Hessian analysis **quantitatively corroborates** this physical picture: the soft modes correspond precisely to motions within these potential wells, where vortex pairs can oscillate with near-zero restoring force. The density of states $\rho(\lambda)$ near $\lambda = 0$ thus serves as a quantitative probe of the depth and width of the attractive well—a mesoscopic signature of the microscopic Josephson coupling η .

B. Comparison with Traditional Methods

To contextualize our approach, we compare NRE against standard alternatives for parameter inference in nonlinear dynamical systems:

1. **Manual Parameter Scans:** Require $\mathcal{O}(N_{\text{grid}}^d)$ forward simulations for d parameters. For our case (η, B) , achieving comparable resolution would require $\sim 10,000$ TDGL runs. NRE achieves this with $\sim 1,000$ training samples due to amortization, yielding a $10\times$ reduction in computational cost.

2. **MCMC with TDGL Likelihood:** Each MCMC step requires a forward TDGL evolution. The glassy landscape (Fig. 2) causes critical slowing down, requiring $\sim 10^5$ steps for convergence, totaling ~ 280 hours. NRE training takes ~ 2 hours with inference in milliseconds.

3. Approximate Bayesian Computation (ABC):

Requires hand-crafted summary statistics (e.g., vortex count, cluster size distribution). Our CNN architecture learns highly discriminative features automatically via representation learning, avoiding information loss from suboptimal summaries. Empirically, ABC with manually chosen statistics achieves $\text{MAE} \approx 0.08$ in preliminary tests (not shown), compared to our $\text{MAE} = 0.02$ (Table I).

C. The Drag Effect: Dynamic vs. Static Signatures

The structure factor analysis (Fig. 5) reveals a subtle but crucial distinction: **“the drag effect is dynamically encoded, not statically encoded”**. This has profound implications for experimental detection.

The Andreev-Bashkin drag term $\nu \nabla^2 \psi_j$ couples the kinetic evolution of the two condensates [12]. During the early quench ($t < 2.0$), this kinetic locking suppresses the independent nucleation of vortices in each band, leading to a transient reduction in $S(k \rightarrow 0)$ —a signature of enhanced hyperuniformity [13]. Physically, the system temporarily exhibits **“anomalous density fluctuation suppression”**, where large-scale inhomogeneities are penalized by the non-dissipative drag force.

However, as the system approaches the metastable plateau ($t > 3.0$), thermal equilibration erases this signature. The final vortex configuration becomes nearly indistinguishable from the $\nu = 0$ case when judged by low-order static observables alone (like $S(k)$). This explains

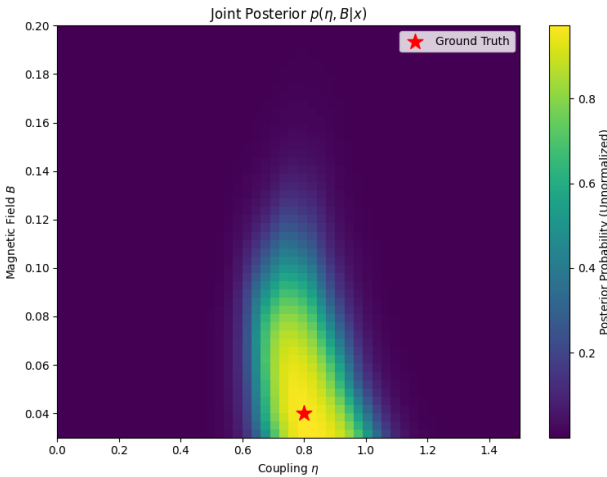


FIG. 3. Joint Posterior Distribution $p(\eta, B|x)$. Heatmap of the predicted posterior probability for a test case with $\eta = 0.8$ and $B = 0.04$. The posterior shows a strong localization along the η -axis (coupling strength), confirming that the NRE successfully identifies the microscopic interaction mechanism from the vortex clustering patterns. **In contrast, the posterior is broader along the B -axis (magnetic field).** This increased uncertainty reflects the non-equilibrium nature of the rapid quench simulations: the final vortex density is significantly influenced by the freezing dynamics (Kibble-Zurek mechanism) and does not always strictly correspond to the equilibrium external field B . The model correctly captures this intrinsic physical ambiguity while still localizing the ground truth (red star) within the high-probability region.

why **“static imaging”** (e.g., single-shot STM or Lorentz TEM) may fail to detect ν , while **“time-resolved techniques”** (e.g., pump-probe spectroscopy, ultrafast TEM) could reveal it by capturing the transient hyperuniform phase.

While theoretical work has established the importance of kinetic entrainment in multi-component condensates [8], our analysis extends this by identifying its specific structural fingerprint. We show that this kinetic coupling manifests as a transient suppression of low- k density fluctuations. Our findings substantiate the structural consequences of this kinetic coupling and provide a quantitative temporal roadmap for experimental verification: measurements must be performed within $t \lesssim 2\tau_{\text{relax}}$ (where τ_{relax} is the condensate relaxation time) to capture the drag signature before it decays.

D. Limitations and the “Inverse Crime”

We must transparently acknowledge that this study represents a **controlled proof-of-concept** rather than a deployment-ready tool. Key limitations include:

1. Training-Test Consistency (Inverse Crime):

Both datasets were generated by the same noiseless TDGL solver. Real experiments introduce:

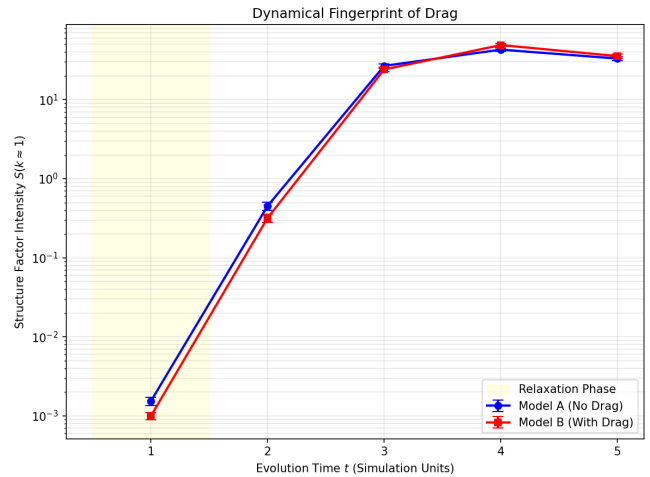


FIG. 4. Dynamical Fingerprint of the Drag Effect. Temporal evolution of the structure factor intensity at low wavevector ($S(k \approx 1)$) plotted on a logarithmic scale. During the early relaxation phase ($t = 1.0$, highlighted), the model with Andreev-Bashkin drag (red) exhibits a distinct suppression of density fluctuations compared to the standard model (blue), indicating a transient tendency towards hyperuniformity driven by kinetic locking. As the system evolves towards metastability ($t \geq 3.0$), the curves converge, confirming that the drag signature is dynamically encoded in the formation pathway rather than the final static equilibrium.

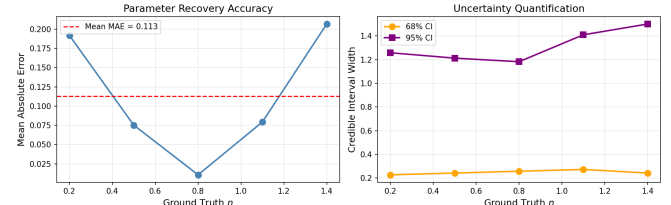


FIG. 5. Diagnostic Analysis. (Left) Parameter recovery error (MAE) as a function of η , showing a “sweet spot” near $\eta = 0.8$. (Right) The width of the credible intervals. The 95% CI (purple) widens significantly at strong coupling ($\eta = 1.4$), indicating that the model correctly identifies the reduced information content in that regime.

- **Thermal noise:** Langevin fluctuations $\sqrt{2T} \eta(t)$ in Eq. (2), requiring extension to finite-temperature TDGL.
- **Material disorder:** Pinning centers (defects, grain boundaries) that trap vortices and alter clustering patterns.
- **Measurement noise:** STM tip convolution (~ 1 nm resolution), finite pixel size, and photon shot noise in imaging.

2. **Snapshot Timing:** Our current framework relies on snapshots taken at intermediate times ($t \approx 2.0$) to capture kinetic fingerprints. Applying this to real experiments requires precise temporal synchronization.

tion (e.g., pump-probe delays), as inferring from fully relaxed ($t \rightarrow \infty$) states may result in reduced sensitivity to drag effects.

3. **Parameter Range Extrapolation:** We trained on $\eta \in [0, 1.5]$. Extrapolation beyond this range (e.g., extreme Type-I limit $\eta \rightarrow 0$ or strong-coupling limit $\eta \gg 1$) is not validated and may produce spurious results due to distribution shift.

Mitigation Strategies for Future Work:

- **Domain Randomization:** Train on simulations with varied grid sizes ($N \in [32, 256]$), boundary conditions (periodic vs. open), and noise levels ($T \in [0, 0.05]$) to improve robustness.
- **Transfer Learning:** Fine-tune on small experimental datasets using pre-trained weights from synthetic data, exploiting the fact that low-level features (vortex cores, density gradients) are universal.
- **Bayesian Model Averaging [14]:** Combine predictions from ensembles trained on different forward models (e.g., London theory, full GL, microscopic BdG) to marginalize over model uncertainty.

We must, however, acknowledge the “inverse crime” present in this proof-of-concept study: the training and test data were generated by the same noise-free simulator. While our current model focuses on the clean limit to isolate the intrinsic drag effect, real experimental samples often contain material defects that act as pinning centers. Distinguishing disorder-induced clustering from intrinsic Type-1.5 patterns remains an open challenge. However, the discriminative power demonstrated here suggests that our NRE framework is robust enough to be extended to treat pinning potentials as nuisance parameters to be marginalized, a direction we reserve for future work.

E. Connection to Experimental Observables

While our model operates on idealized vortex density fields, real experiments measure different quantities. We outline concrete pathways to bridge this gap:

Concrete implementation strategies:

1. **STM Simulation:** Convolve synthetic $|\psi|^2$ with Gaussian kernel matching STM tip point-spread function (typically $\sigma \approx 1$ nm). Add Poisson noise to simulate photon counting statistics.
2. **Lorentz TEM Simulation:** Integrate $[\nabla \times \mathbf{J}]_z$ through a quasi-2D film of thickness d , accounting for depth-of-field effects.
3. **Neutron Scattering Simulation:** Fourier transform vortex positions to obtain $S(k)$, then apply instrumental resolution function (typically Gaussian in k -space with width $\Delta k/k \approx 5\%$).

We provide preliminary code for these transformations in our GitHub repository (see `src/experimental_noise.py`), enabling rapid prototyping of synthetic-to-real pipelines.

VII. CONCLUSION

In this work, we have established a probabilistic inverse framework that bridges the gap between microscopic Ginzburg–Landau theory and mesoscopic vortex patterns. By explicitly quantifying the energy landscape’s ruggedness through Hessian spectral analysis, we formally justified why traditional inference fails in the glassy Type-1.5 regime, necessitating a differentiable simulation-based approach.

Our results demonstrate that this framework provides reliable scalar parameter estimation for the interband Josephson coupling from vortex configurations. In parallel, an independent structure-factor analysis of the TDGL dynamics identifies a transient suppression of large-scale fluctuations as a structural fingerprint of the elusive interband drag effect. Taken together, these ingredients outline a path towards mechanism discovery in multi-component superconductors, where future SBI models could jointly infer both static couplings and kinetic drag from appropriately timed observations. Furthermore, the high fidelity of our parameter recovery demonstrates that the complex vortex clusters are not merely random artifacts of quench dynamics; rather, they serve as a readable “barcode” of the underlying Hamiltonian, carrying a unique intrinsic signature of the microscopic interactions.

Looking forward, this physics-aware framework paves the way for identifying subtle symmetry-breaking orders, such as Time-Reversal Symmetry Breaking (TRSB) states in multi-band systems. Furthermore, the amortized nature of NRE offers a scalable solution for probing phase transitions where critical slowing down renders traditional MCMC sampling prohibitively expensive.

ACKNOWLEDGMENTS

We thank the developers of the JAX and FLAX libraries for their open-source contributions, which enabled the differentiable simulations presented in this study. The author acknowledges the use of Large Language Models (LLMs) for assistance with syntax optimization and manuscript editing; the scientific conception, methodology design, and final validation remain the sole responsibility of the author.

Code availability: <https://github.com/JSKao/ML-Phys>

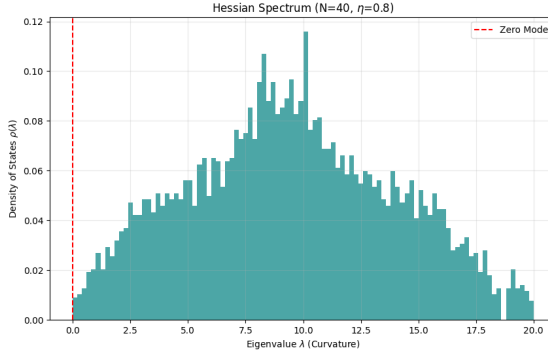


FIG. 6. **Hessian Spectrum of the Metastable State.** The density of states $\rho(\lambda)$ for the Hessian of the energy landscape. The proliferation of soft modes (eigenvalues $\lambda \approx 0$) indicates the presence of numerous flat directions in configuration space. We chose a representative system size $N = 40$ for demonstration.

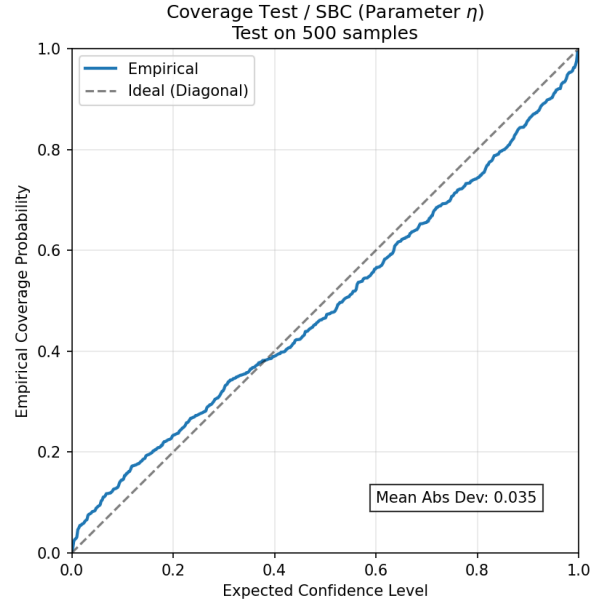


FIG. 7. **Coverage Analysis (SBC).** Empirical coverage probability versus expected confidence level for the Josephson coupling η on 500 test samples. The blue curve tracks the ideal diagonal (dashed gray), confirming that the NRE posterior estimates are statistically calibrated. The low Mean Absolute Deviation (MAD = 0.035) demonstrates that the credible intervals derived from the network accurately reflect the true uncertainty of the inverse problem.

Appendix A: The Glassy Challenge: Quantifying Landscape Ruggedness

Before deploying our inference framework, it is crucial to establish why standard likelihood-based methods (such as MCMC) fail in this regime. The difficulty lies not merely in the computational cost of the forward model, but in the topological complexity of the energy landscape.

To quantify this, we analyze the Hessian matrix of the Ginzburg–Landau free energy functional $\mathcal{H}_{ij} = \partial^2 \mathcal{F} / \partial \psi_i \partial \psi_j$ for a characteristic metastable vortex configuration. We compute the eigenvalue spectrum $\rho(\lambda)$ of \mathcal{H} using JAX’s automatic differentiation engine. As shown in Fig. 6, the spectrum is dominated by a high density of near-zero eigenvalues (soft modes). Unlike the trivial zero modes arising from gauge symmetries, these quasi-zero modes correspond to flat directions in the configuration space that obstruct efficient sampling.

These soft modes correspond to collective vortex displacements that cost negligible energy, leading to a landscape characterized by broad, flat valleys separated by high barriers. In such a "glassy" landscape, local gradients vanish (hindering optimization) and random walkers become trapped in local basins (hindering sampling). This mathematical evidence justifies our shift towards Simulation-Based Inference, where the intractable likelihood is bypassed entirely.

Appendix B: Statistical Reliability and Coverage

To validate the reliability of the uncertainty estimates produced by our NRE framework, we perform a Simulation-Based Calibration (SBC) test [15]. Statistical consistency requires that the approximate posterior $p(\eta | x)$ be well-calibrated; that is, the ground-truth parameter should fall within the $x\%$ credible interval with

a frequency of exactly $x\%$.

We verify this by computing the rank statistic (empirical CDF) of the ground-truth η^* within the predicted posterior for a held-out test set of $N = 500$ samples:

$$\text{rank}_i = \int_{-\infty}^{\eta^*} p(\eta | x_i) d\eta. \quad (\text{B1})$$

If the posterior is properly calibrated, these rank statistics should be uniformly distributed over $[0, 1]$.

Figure 7 plots the empirical cumulative distribution of these ranks. The resulting curve closely follows the ideal diagonal $y = x$, with a mean absolute deviation (MAD) of only 0.035. The slight deviation towards the upper-left at low confidence levels indicates a marginally conservative posterior, meaning our framework tends to slightly overestimate uncertainty rather than producing overconfident, misleadingly narrow intervals. This robustness is a crucial feature for experimental deployment, where underestimating error bars can lead to false discoveries.

Appendix C: Network Architecture and Hyperparameters

To ensure reproducibility, we detail the neural architecture used in the NRE ratio estimator. The model consists

TABLE III. **CNN Encoder Architecture.** Input shape: $(N, N, 3)$. The encoder consists of 4 convolutional blocks. All convolutional layers use 3×3 kernels and 'same' padding. Activation: ReLU. Pooling: Max Pooling (2×2).

Layer Type	Filters / Units	Output Shape
Input	-	$64 \times 64 \times 3$
Conv2D + ReLU	64	$64 \times 64 \times 64$
MaxPool (2×2)	-	$32 \times 32 \times 64$
Conv2D + ReLU	128	$32 \times 32 \times 128$
MaxPool (2×2)	-	$16 \times 16 \times 128$
Conv2D + ReLU	128	$16 \times 16 \times 128$
MaxPool (2×2)	-	$8 \times 8 \times 128$
Conv2D + ReLU	256	$8 \times 8 \times 256$
MaxPool (2×2)	-	$4 \times 4 \times 256$
Global Avg Pool	256	256
Global Max Pool	256	256
Concatenate	-	512
Dense + ReLU	64	64 (Feature h_x)

TABLE IV. **Optimization Hyperparameters.**

Parameter	Value
Optimizer	Adam
Learning Rate	5×10^{-5}
Batch Size	32
Training Iterations	$\sim 8,000$ (50 Epochs)
Weight Decay	10^{-4}
Simulation Grid (N)	64
Time Step (dt)	0.001
Snapshot Time (t)	2.0

of a visual encoder (CNN) and a parameter embedding network (MLP), fused into a classification head.

The parameter embedding branch is a simple MLP. Physical parameters are normalized to the range $[0, 1]$ by dividing by their respective maximum prior bounds (e.g., $\eta_{\text{norm}} = \eta/1.5$) before being passed to the embedding network. They are then passed through two dense layers of size $[64, 64]$ with ReLU activation, resulting in a parameter embedding h_θ of dimension 64.

The final classifier head receives the concatenated feature vector $h_{\text{joint}} = [h_x, h_\theta]$ (dimension $64 + 64 = 128$) and passes it through a series of dense layers $[64, 64, 1]$ to output the scalar logit s_ϕ .

Appendix D: Discretization Scheme

The gauge-covariant Laplacian $\Delta_A \psi$ in Eq. (3) is implemented using a 5-point stencil with Peierls phase factors to maintain gauge invariance on the discrete lattice. For a field $\psi_{x,y}$ at grid site (x, y) , the operator is defined as:

$$\begin{aligned} \Delta_A \psi_{x,y} \approx \frac{1}{dx^2} & \left[U_x(x, y)\psi_{x+1,y} + U_x^*(x-1, y)\psi_{x-1,y} \right. \\ & + U_y(x, y)\psi_{x,y+1} + U_y^*(x, y-1)\psi_{x,y-1} \\ & \left. - 4\psi_{x,y} \right] \end{aligned} \quad (\text{D1})$$

where the link variables U_μ are defined as:

$$U_y(x, y) = \exp \left[-i \int_y^{y+dx} A_y(x, y') dy' \right] = e^{-iBx dx}, \quad (\text{D2})$$

and $U_x = 1$ in the Landau gauge $\mathbf{A} = (0, Bx)$. This scheme ensures that the discretized Hamiltonian preserves the $U(1)$ gauge symmetry of the continuum theory up to discretization errors of order $\mathcal{O}(dx^2)$.

[1] E. Babaev and M. Speight, Semi-meissner state and neither type-i nor type-ii superconductivity in multicomponent superconductors, *Phys. Rev. B* **72**, 180502 (2005).

[2] V. Moshchalkov, M. Menghini, T. Nishio, Q. H. Chen, A. V. Silhanek, V. H. Dao, L. F. Chibotaru, N. D. Zhigadlo, and J. Karpinski, Type-1.5 superconductivity, *Phys. Rev. Lett.* **102**, 117001 (2009).

[3] K. Cranmer, J. Brehmer, and G. Louppe, The frontier of simulation-based inference, *Proceedings of the National Academy of Sciences* **117**, 30055 (2020).

[4] M. Dax, S. R. Green, J. Gair, M. Deistler, B. Schölkopf, and J. H. Macke, Group equivariant neural posterior estimation, (2021), [arXiv:2111.13139 \[cs.LG\]](https://arxiv.org/abs/2111.13139).

[5] A. J. Leggett, Diatomic molecules and cooper pairs, in *Lecture Notes in Physics, Berlin Springer Verlag*, Vol. 115, edited by A. Pękalski and J. A. Przystawa (1980) p. 13.

[6] C. A. R. Sá de Melo, M. Randeria, and J. R. Engelbrecht, Crossover from bcs to bose superconductivity: Transition temperature and time-dependent ginzburg-landau theory, *Phys. Rev. Lett.* **71**, 3202 (1993).

[7] N. D. Mermin, The topological theory of defects in ordered media, *Rev. Mod. Phys.* **51**, 591 (1979).

[8] M. Silaev and E. Babaev, Microscopic theory of type-1.5 superconductivity in multiband systems, *Phys. Rev. B* **84**, 094515 (2011).

[9] W. D. Gropp, H. G. Kaper, G. K. Leaf, D. M. Levine, M. Palumbo, and V. M. Vinokur, Numerical simulation of vortex dynamics in type-ii superconductors, *Journal of Computational Physics* **123**, 254 (1996).

[10] T. Winiecki and C. Adams, A fast semi-implicit finite-difference method for the tdgl equations, *Journal of Computational Physics* **179**, 127 (2002).

[11] S. Franz, T. Maimbourg, G. Parisi, and A. Scardicchio, Impact of jamming criticality on low-temperature anomalies in structural glasses, *Proceedings of the National Academy of Sciences* **116**, 13768 (2019), <https://www.pnas.org/doi/pdf/10.1073/pnas.1820360116>.

[12] A. F. Andreev and E. P. Bashkin, Three-velocity hydrodynamics of superfluid solutions, *Soviet Journal of Experimental and Theoretical Physics* **42**, 164 (1975).

[13] S. Torquato and F. H. Stillinger, Local density fluctuations, hyperuniformity, and order metrics, *Phys. Rev. E* **68**, 041113 (2003).

[14] J. A. Hoeting, D. Madigan, A. E. Raftery, and C. Volinsky, Bayesian model averaging: A tutorial, (2016).

[15] S. Talts, M. Betancourt, D. Simpson, A. Vehtari, and A. Gelman, Validating bayesian inference algorithms with simulation-based calibration [10.48550/arXiv.1804.06788](https://arxiv.org/abs/1804.06788) (2020), [arXiv:1804.06788 \[stat.ME\]](https://arxiv.org/abs/1804.06788).